Static friction between rigid fractal surfaces

Fernando Alonso-Marroquin, Pengyu Huang, Dorian A. H. Hanaor, E. A. Flores-Johnson, Gwénaëlle Proust,
Yixiang Gan, and Luming Shen

School of Civil Engineering, The University of Sydney, Sydney, New South Wales 2006, Australia

Using spheropolygon-based simulations and contact slope analysis, we investigate the effects of surface topography and atomic scale friction on the macroscopically observed friction between rigid blocks with fractal surface structures. From our mathematical derivation, the angle of macroscopic friction is the result of the sum of the angle of atomic friction and the slope angle between the contact surfaces. The latter is obtained from the determination of all possible contact slopes between the two surface profiles through an alternative signature function. Our theory is validated through numerical simulations of spheropolygons with fractal Koch surfaces and is applied to the description of frictional properties of Weierstrass-Mandelbrot surfaces. The agreement between simulations and theory suggests that for interpreting macroscopic frictional behavior, the descriptors of surface morphology should be defined from the signature function rather than from the slopes of the contacting surfaces.

I. INTRODUCTION

Solid surfaces of natural and manufactured materials tend to exhibit irregularities across multiple scales. Typical surface structures consist of hierarchical asperities exhibiting statistical self-affinity, across a range of length scales covering several orders of magnitude [1–3]. Conventional surface descriptors of mean roughness or gradient are generally dominated respectively by features at the highest scale or finest scale. For this reason fractal analysis is increasingly used as a meaningful cross-scale descriptor to characterize and define surface structures and model interfacial contact mechanics [4–7]. Indeed, it has been shown for elastic and viscoelastic systems that understanding and interpreting frictional interactions at static or low-velocity conditions necessitate the consideration of the multiscale nature of solid interfaces [8–10].

Frictional phenomena at material interfaces are known to be governed both by the atomic interactions occurring at bulk and surface regions in materials and by the multiscale surface structures at regions of apparent contact [11,12]. A linear relationship between normal load and frictional force, captured by the friction coefficient μ, following Amonton's law, is sufficient for the description of most macroscopically observed systems. However, at the nanoscale, observed frictional forces arising from atomic-scale mechanisms often deviate from this linear relationship with nonlinearity between applied load and frictional force [13]. The frictional interactions at the nanoscale are further strongly governed by coupled surface chemistry and temperature [14,15]. Integrating atomistic mechanisms of friction with cross-scale surface structures and bulk deformation modes has proven challenging and has been the subject of significant research efforts [11,16,17]. Recent research has revealed the existence of a complex interplay of atomic stick-slip friction, surface corrugations, and temperature [18], highlighting the need for further studies towards a multiphysics understanding of friction at rough surfaces.

When two nominally flat surfaces interact, true contact takes place through a limited number of discrete points determined by the multiscale structures of the surfaces. The area of true contact is thus generally much smaller than the nominal interfacial contact area between the two surfaces [19,20]. Following pioneering work by Archard [21], it has been shown through analytical models and experimentation that the true contact area at the interface of two self-affine surfaces is linearly proportional to the normal force applied on the two solids [22–27]. Frictional force is often considered as linearly proportional to the true contact area [28–30]. This can be rationalized by considering friction to arise from the rupturing of bonds at regions of true contact. Following these two proportionalities, the ubiquitous friction-load linearity of Amonton's law is observed. The original idea of Archard was later extended by several authors (Yang and Komvopoulus [31], Ciavarella *et al.* [32], and Gao and Bower [33]), who introduced fractal models for the statistical description of the self-affinity of roughness. These models focused on the fractal properties of the contact areas and the number of contact spots, while the connection between surface roughness and actual friction has been explored only recently [12].

With the evolution of nanoscale measurement techniques, an increasing number of experimental studies have investigated the atomistic origins of friction in a range of systems by means of friction force microscopy methods [13,34,35]. Suh and Sin [10] argued that the deformation and ploughing of surface asperities account only for a part of the observed frictional force and that there is a significant contribution due to atomic-scale mechanisms acting at the flat portions of the sliding surface. Studies of these atomic mechanisms have shown that friction can dramatically depend on the chemical and atomic nature of surfaces [36,37], with the observed friction coefficient often being load dependent [36,38].

The main conclusion that can be drawn from both surface topography characterization and atomic friction analysis is that both surface structure fractality and atomic-scale effects need to be considered in the study of the macroscopic frictional phenomena. The motivation of this paper is to shed light on connections between surface topography and static friction at interfaces of fractal surfaces exhibiting negligible deformation. In this work we consider a fractal topography of rigid asperities, with microscopic effects captured by Amonton-type atomic friction. In Sec. II we derive a theoretical

model to predict the static friction as a function of the atomic friction coefficient and surface topography using the concept of a signature function. This function is a measure of the angle of all possible contact slopes between two rough surfaces. In Sec. III we calculate the signature function of rigid fractal Koch surfaces and in Sec. IV we test the theory by means of a spheropolygon-based model that simulates the interaction between rigid surfaces with complex multiscale topographies. We also provide scenarios where the friction can be controlled to achieve large values by changing topography parameters only. We extend our description to random Weierstrass-Mandelbrot-type fractal surfaces, which describe natural surfaces more accurately in Sec. V. We summarize in Sec. VI.

II. FRICTION BETWEEN RIGID SURFACES

Static friction at the interface of rigid surfaces arises from the interlocking of surface asperities and from atomic friction occurring at contact regions of these asperities. Shear-driven displacement requires asperities on one surface to climb over those on an opposing surface [28]. The shear force required to achieve this displacement is a function of the slope of the asperities at the contact points. In Sec. II A we introduce a signature function, which returns the slope of the interface at regions of true contact (subsequently referred to as contact slope) at a given relative displacement of the contacting surfaces. The macroscopic friction can be examined as a function of the contact slope and atomic friction.

A. Calculation of the contact slope and signature function

To examine macroscopic friction at the interface of two contacting surfaces we determine all possible contact slopes that are consistent with the geometrical constraints of the rigid bodies. An illustration of the process involved in finding active contact points is shown in Fig. 1. First we consider in our description any possible position of the top surface relative to the bottom one as follows: Given the profile of two continuous contacting surfaces and their relative displacement x_{ofs}, surface points involved in a contact event can be obtained by finding the minimal distance d_{min} between the surfaces. Contact slopes are then calculated by taking the derivative of the surface profiles at the individual contact points. Since the contact slopes between two contacting surfaces are dependent on their relative position, all the possible contact slopes $\theta(x_{ofs})$ can be calculated using the processes shown below. The values
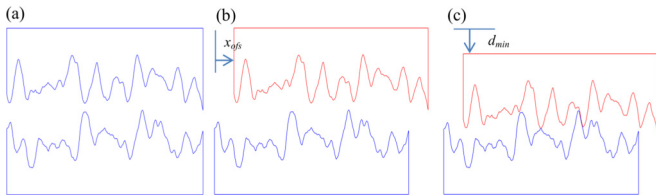

FIG. 1. (Color online) Evaluation of contact points. (a) One surface, defined by $f(x)$, is placed above the other, defined by $g(x)$. (b) The upper surface has been shifted horizontally by x_{ofs}. (c) The contact points are obtained after moving the top block by the minimum distance d_{min} between the surfaces.

of x_{ofs} are taken from 0 to $x_{ofs\,max}$. For periodic surfaces, $x_{ofs\,max}$ can be taken as one wavelength of the surface, while for nonperiodic surfaces, $x_{ofs\,max}$ is chosen as a half of the surface length to take into account a large enough number of possible contact slopes.

Consider one block with a surface profile $g(x)$ above the other with a surface profile $f(x)$. We assume that $g(x) > f(x)$ for all x such that the two surfaces do not intersect. The relative position between them can be described as the shifted distance of the upper block by a horizontal offset x_{ofs} [Fig. 1(b)]. The vertical distances between the two surfaces for any x and x_{ofs} can be defined as

$$d(x,x_{ofs}) = g(x - x_{ofs}) - f(x). \qquad (1)$$

Let us define $d_{min}(x_{ofs}) = \min_{x_{ofs} \leqslant x \leqslant L_b}\{d(x,x_{ofs})\}$ as the shortest vertical distance between the two surfaces (L_b is the length of the block). Contact points between $g(x - x_{ofs})$ and $f(x)$ are created by moving down the surface $g(x - x_{ofs})$ by d_{min}. Contact surfaces are rigid and the blocks do not rotate, thus the existence of more than one contact point is rare. The x coordinate of all contact points can be calculated from the function

$$g(x - x_{ofs}) - d_{min}(x_{ofs}) - f(x) = 0. \qquad (2)$$

If the solutions of this equation are $x_1, \ldots, x_N$ the contact points are given by $[x_1, f(x_1)], \ldots, [x_n, f(x_N)]$, where N is the number of contact points. An illustration of the method used to define the points of contact is shown in Fig. 1(c).

If the surfaces are smooth, the slopes of the two surfaces at the contact points are the same. The maximum value among the identified contact slopes along the contact points is the slope of interest, as this represents the critical obstacle to the sliding of the upper surface. Therefore, the contact slope θ, given the surface profiles and the relative position, can be defined by the maximum of the derivatives at either surface

$$\theta(x_{ofs}) = \max[f'(x_1), \ldots, f'(x_N)]. \qquad (3)$$

The function $\theta(x_{ofs})$ is referred to as the signature function and describes the relationship between the contact slope and the relative positions between two surfaces. To predict the maximum static friction, we assume that the upper surface is shifted in its horizontal position to yield the maximum contact slope among all possible slopes obtained from all relative positions. In practice, the surfaces may slide with respect to each other until they reach a local maximal slope, so the resulting friction is likely to be smaller than the maximal value obtained from the signature function. We will find that for the fractal Koch surfaces (described in Sec. III) the surfaces can vary across all possible relative positions. Thus the use of the maximal slope angle and atomic friction will be appropriate for the prediction of the macroscopic friction. Later in Sec. V we discuss the cases where the contact surfaces may not reach the maximal contact slope and we introduce a statistical description of static friction.

B. Calculation of contact forces

The total friction force can be calculated by superposing the contributions of the contact slope and atomic friction. As illustrated in Fig. 2, a surface sheared over the top of another
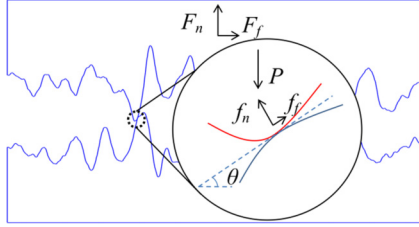
FIG. 2. (Color online) Contact point with local normal and friction forces (f_n and f_f); P is the downward force at the contact point due to the applied force on the block, which is equal to F_n if there is only one contact point.

has to overcome the angle θ and also the atomic friction force acting in the tangential orientation to the contact slope at the asperities' surfaces.

Following the ubiquitously applied Amonton-Coulomb friction law, the macroscopic friction coefficient μ linearly correlates the overall frictional force F_f with the applied normal force F_n:

$$|F_f| \leqslant \mu F_n. \tag{4}$$

Similarly, for the asperity-localized forces shown in Fig. 2, where μ_a is the atomic friction coefficient, the local frictional force is calculated following Amonton's law:

$$|f_f| \leqslant \mu_a f_n. \tag{5}$$

The macroscopic friction can be evaluated from the summation of local forces at individual contact points. Thus μ can be expressed in terms of μ_a and θ:

$$\phi = \theta_a + \theta, \tag{6}$$

where $\theta_a = \tan^{-1}\mu_a$ and the angle of macroscopic friction is defined as $\phi = \tan^{-1}\mu$. Through this equation, the macroscopic friction takes into account the combined effect of the contact slope θ due to morphology and of θ_a that describes the atomic effects on friction. We define here the apparent friction as the contribution of the morphology to the total static friction and the quantity $\tan\theta$ will be referred to here as the coefficient of apparent friction.

III. SIGNATURE FUNCTION OF FRACTAL KOCH SURFACES

We use a commonly studied fractal surface structure, namely, the triadic Koch surface [39–41], to examine the relationship between friction and surface structure. The initial polygon used to generate the Koch surfaces consists of a series of isosceles triangles of base λ and angle α as shown in Fig. 3. Following similar work by Lung *et al.* [41], Koch-type surfaces are iteratively generated as follows: In each iteration, each line segment is divided into three equal segments; the middle segment is replaced by an isosceles triangle with a unit slope α. By increasing the value of α, we increase the roughness and fractality of the surface. The surfaces will have further levels of triangular features as the number of iterations increases. This leads to an increase of the surface slope by α at each iteration (see Fig. 3). Koch surfaces are denoted by K_n, where n represents the number of iterations used to generate surface
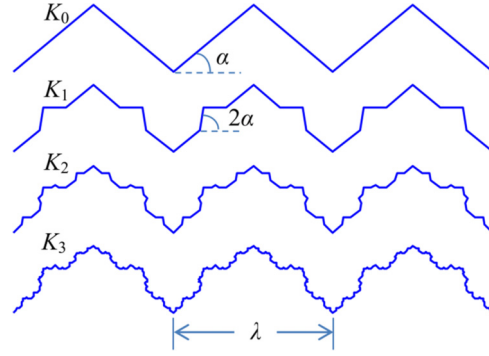

FIG. 3. (Color online) Koch surfaces for different numbers of iterations.

features, as illustrated in Fig. 3. As surfaces generated with $n \geqslant 1$ and $\alpha > 60°$ exhibit overlapping surface features, we study only surfaces with $\alpha \leqslant 60°$ in the present work. To investigate the effect of surface roughness on static friction, Koch surfaces were generated using the morphological parameters shown in Table I.

As Koch surfaces are piecewise continuously differentiable functions, the slopes of both surfaces at the contact point would be the same for edge-edge contact. The contact slope for vertex-edge and for vertex-vertex contact is taken as the slope of the edge and the average between the slopes of vertices, respectively. The slope of the vertex is resolved as the average between the slopes of its adjacent edges. The resulting signature functions are shown in Fig. 4. Since the Koch surfaces generated are periodic, the domain of the function should be selected between 0 and the wavelength λ. The surface profile height and the signature function are both expected to scale linearly with α. Thus, it is sufficient to plot θ/α as a function of the normalized offset $x_{\rm ofs}/\lambda$. The static friction coefficient, represented by the friction angle, can be predicted as the sum of $\theta_{\rm max,th}$ and θ_a using Eq. (6), where $\theta_{\rm max,th}$ is the maximal value of the signature function and θ_a is the atomic friction.

It is worth noting that higher values of surface roughness do not necessary imply higher friction angles. Indeed, the K_1 Koch surfaces are rougher than the K_0 ones and yet they have the same friction angle. We also note that in the case of vanishing atomic friction the maximal angle of the slope is not necessarily the same as the angle of friction. Indeed, the signature of the K_2 surface in Fig. 4 returns a maximal contact slope of 2α, while the maximal slope of the curves is 3α. This

TABLE I. Input parameters for producing Koch surfaces.

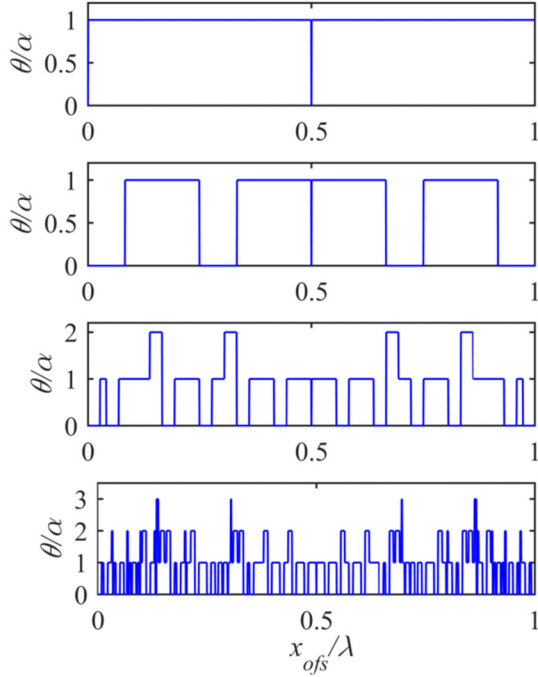| Symbol	Unit	Description	Value
α	deg	slope of the triangles	5–50 for K_0 and K_1
			5–45 for K_2
			5–25 for K_3
L_b	m	length of the block	0.2
λ	m	wavelength	0.01
h	m	height of the block	0.01
K_i		i is the number of iterations	0–3

FIG. 4. (Color online) Signature function of Koch surfaces for $\alpha = 5°$. The plots from top to bottom represent the signature functions for the surfaces for K_0, K_1, K_2, and K_3 respectively.

is because pairs of surface features yielding contact slopes of 3α never enter into contact due to geometrical constraints; the blocks cannot overlap each other. Similarly, K_3 surfaces have a maximum contact slope of 3α. This suggests that rather than the description of individual surface profiles, the signature function, accounting for all possible contact slopes, is a more appropriate tool for the interpretation of macroscopic friction between surfaces.

IV. SPHEROPOLYGON-BASED SIMULATIONS OF FRICTION BETWEEN FRACTAL SURFACES

The interaction between rigid surfaces is simulated using spheropolygons. These geometrical objects are obtained from the Minkowski sum of polygons and spheres. Spheropolygons were proposed for rigid-body simulations by Pournin and Liebling [42]. The method was later extended by Alonso-Marroquin *et al.* to include both conservative and dissipative interactions and multiple contacts between nonconvex particles [43–45]. The forces at the contact points are calculated from the overlapping distance between sphere radii instead of polygons, which simplifies the calculation of contact force. The computational time is further reduced using a combination of the Verlet distance concept and neighbor tables that is tailored for this particular case of geometrical objects [43–46]. While the major application of this method has been the investigation of granular flow [47] and pedestrian flow [48], it is shown that particles generated by Minkowski sums are promising in the investigation of the effects of friction and rheology due in flat and nonconvex particles [49,50]. Here we exploit further the effect of nonconvexity on friction by using nonconvex spheropolygons with complex (fractal) topography.
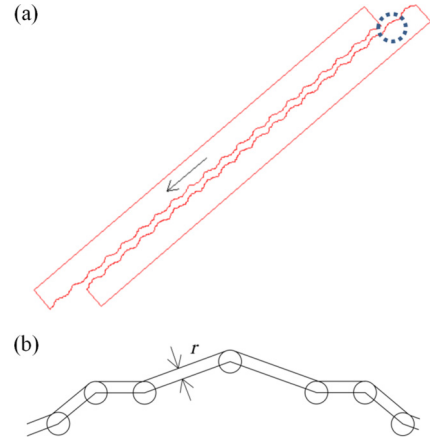

FIG. 5. (Color online) (a) Snapshot of the simulation of blocks with fractal Koch surfaces using the method of tilting. (b) Magnification of the circular area in (a) to show the disk sweeping around the surface and its spheroradius r.

A. Spheropolygon-based modeling for rigid surfaces

For validation purposes we compare our analytical model of static friction with spheropolygon-based simulations of rigid blocks generated with fractal Koch surfaces. In these simulations, the angle of static friction is calculated by tilting the blocks. As illustrated in Fig. 5, the lower block is subjected to rotation at a constant angular velocity while the upper block is free to move. The angle of friction ϕ is measured as the angle at which the upper block starts to slide continuously relative to the lower block. The tangent of ϕ corresponds to the macroscopic coefficient of friction μ, here referred to as the coefficient of static friction. To avoid time-dependent effects, the angular velocity of the rotation is set at a relative low speed (0.05 rad/s).

Rigid-body spheropolygon simulations were carried out using SPOLY [43,45], an in-house-developed software package. Each block is represented by a spheropolygon [43,45]. This is generated using a disk with radius r (called here spheroradius) to sweep around the initial polygon resulting in a polygon with smooth vertices [Fig. 5(b)]. Using SPOLY the interaction forces between edges and vertices of the particles in contact are calculated. Subsequently, these forces are included in the equations of motion that are integrated numerically to obtain positions and orientations of the bodies. The contact forces consist of elastic and viscous components [44]

$$\vec{f}^c = \vec{f}_n^e + \vec{f}_t^e + \vec{f}_n^v + \vec{f}_t^v, \qquad (7)$$

where the elastic forces are given as

$$\vec{f}_n^e = -k_n \Delta x_n \vec{n}, \qquad (8)$$

$$\vec{f}_t^e = -k_t \Delta x_t \vec{t}, \qquad (9)$$

where $\vec{n}$ and $\vec{t}$ are the normal and tangential unit vectors, k_n and k_t are the normal tangential stiffness parameters, and Δx_n and Δx_t are the normal and tangential relative displacement between the spheropolygons. The latter is corrected in each time step to satisfy the sliding condition $|\vec{f}_t^e| \leqslant \mu_a f_n^e$.

The viscous forces are given as

$$\vec{f}_n^v = -m\gamma_n v_n \vec{n}, \tag{10}$$

$$\vec{f}_t^v = -m\gamma_t v_t \vec{t}. \tag{11}$$

where $m = m_1 m_2/(m_1 + m_2)$ is the effective mass of the particles with masses m_1 and m_2. The normal and tangential coefficients of damping are given by γ_n and γ_t respectively; v_n and v_t denote the normal and tangential components of the contact velocity.

B. Determination of the simulation parameters

As the spheroradius r can affect the simulation results, its value was minimized such that a further reduction did not yield any observable effect on the resultant frictional interactions. The value of k_n was chosen so that it provides sufficient contact force to avoid penetration between the two surfaces. The value of k_n used in the simulations was taken large enough that a further increase did not affect the results. This regularization is based on experimental and numerical analysis of two sliding blocks [44]. Using the same analysis, the normal stiffness k_t was selected as a fraction of k_n (1/10). The normal damping coefficient γ_n and the coefficient of restitution ε_p are correlated by the expression [44]

$$\varepsilon_p = \exp\left[-\frac{\gamma_n}{2}\frac{\pi}{\sqrt{k_n/m_1 - (\gamma_n/2)^2}}\right]. \tag{12}$$

The value of ε_p should not be excessively large as to cause overdamping of the system and also not too small as to produce excessive bouncing between the blocks. In our case, it was established that using $\varepsilon_p = 0.5$ results in a reasonable damped interactions between the blocks. This gives us a normal damping coefficient of $\gamma_n = 929.5$ s^{-1}. The parameter γ_t is related to the relative terminal velocity between the two blocks sliding each other [44]. By comparison with experiments, it was found that the sensibility of the results with γ_t is small if it is taken much smaller that γ_n. Therefore, a small value of γ_t was used in this simulation. Those selected values (Table II) ensure stable and reasonable simulations results.

The sensitivity of the ratio of the length of the block to the wavelength was also studied. The simulation results showed that such sensitivity is very low for periodic surfaces; therefore, a default ratio of 20 was used for both types of surfaces (Table I). The height of the block (as shown in Table I) is taken small enough to reduce the overturning moments that arise just before reaching the maximal contact force.

TABLE II. Input parameters used in SPOLY.

Parameters	K_0, K_1, K_2, K_3 surfaces
k_n (N/m)	6×10^5
k_t (N/m)	6×10^4
γ_n (l/s)	929.5
γ_t (l/s)	4
r (m)	5×10^{-5}
ρ (kg/m^2)	50

C. Simulation results and comparison with theory

Simulations of frictional interactions between two tilting blocks with fractal Koch surfaces were conducted with varied numbers of iterations and α values. In order to study the combined effect of the surface structure and atomic friction, the coefficients of atomic friction were also varied from 0 to 1.

1. Effect of surface roughness

For Koch surfaces, the degree of roughness depends on the number of iterations and the value of α. Simulation results with zero atomic friction were plotted for surfaces generated with different numbers of iterations and values of α as shown in Fig. 6. This was done to investigate the contribution of apparent friction to the total static friction. As expected, the macroscopic friction angle increases monotonically with α. The results for K_0 and K_1 were found to be identical, although K_1 surfaces exhibit a greater value of overall surface slope at finer features, which do not participate in contact events, as predicted by the signature function of these two surfaces. The maximum apparent friction angles for any Koch surfaces are accurately predicted by the derived theory and the simulations as shown by Fig. 6.

Figure 7 shows the time evolution of the friction. The forces F_x and F_y are calculated by summing all the contact forces between the blocks. Then F_n and F_t are obtained by applying the rotation matrix based with the tilted angle at each time step. Plots of $\tan^{-1}(F_t/F_n)/\alpha$ against the relative displacement of the blocks for K_0–K_3 surfaces with $\alpha = 20°$ are shown in Fig. 7, illustrating the changes of frictional forces as the upper block is displaced relative to the lower one. The upper block will initially move to form contact between the first triangular Koch surface elements, requiring sufficient shear force to overcome these features. Subsequently, the surface will either commence sliding or meet a higher-order feature. These results are consistent with our theory given in Sec. II B.
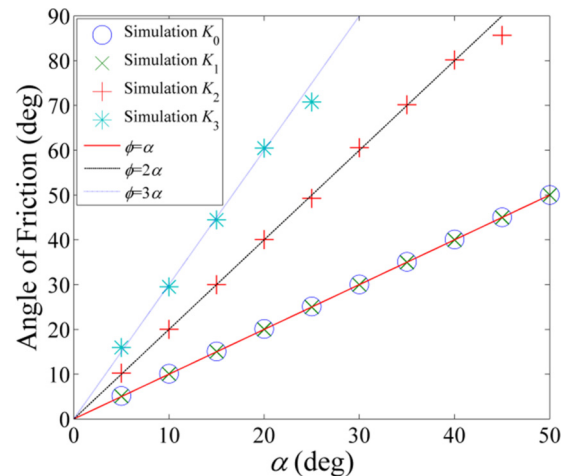

FIG. 6. (Color online) Resulting friction angles in simulations versus the value of α, with zero atomic friction. The lines represent the theoretical result $n\alpha$, where n was obtained from the signature functions for different surfaces.
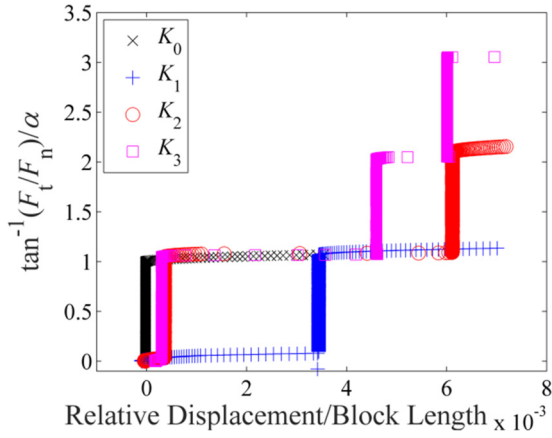
FIG. 7. (Color online) Plot of $\tan^{-1}(F_t/F_n)/\alpha$ against relative displacement divided by L_b for K_0–K_3 for $\alpha = 20°$. The relative displacement is the movement in the tilted direction between the initial centroid of the lower block and the centroid of the upper block.

2. Contribution of atomic friction

The contribution of atomic friction to total static friction was also studied by means of spheropolygon simulations using SPOLY. Results of ϕ for different atomic friction coefficients are shown in Fig. 8. The figure shows that the results are consistent with those obtained from the signature function. In general, the results indicate that the relative contribution of atomic friction is independent of surface roughness and ϕ is linearly proportional to θ_a with a slope of 1.0. From the results, the static friction increases monotonically with atomic friction, until a friction angle of 90°. By comparing the theoretical and simulation results, we found that the predicted effects of the apparent and atomic friction on static friction fit the simulation results reasonably well.

3. Relationship between macroscopic friction and fractal dimension

In this section we examine the relationship between surface fractality, as given by the Hausdorff dimension, and the coefficient of static friction at the interface of two Koch
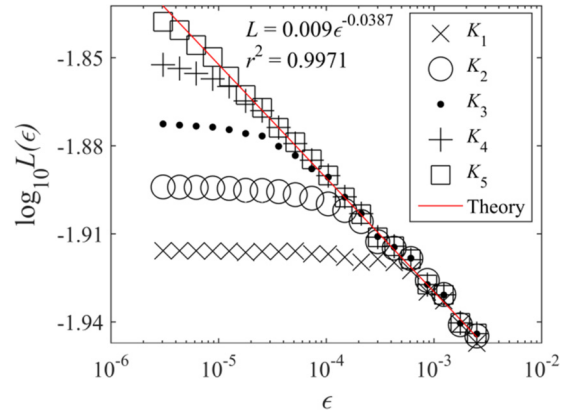

FIG. 9. (Color online) A log-log plot of L against ε for K_1–K_5 surfaces for $\alpha = 30°$.

surfaces. The fractality of these surfaces is evident from the power-law scaling of observed surface profile length with measurement length scale. The fractal dimension of these surfaces can be obtained using the divider method employed to interfaces within a two-dimensional domain [51–53]. The scaling of the total measured length L with ruler length ε follows a power law such that $L(\varepsilon) = F\varepsilon^{1-D}$ as shown in Fig. 9. The linear behavior in the log-log plot of L versus ε is indicative of surface fractality within a certain range of scales. The fractal dimension is obtained from the slope of the line m, as $D = 1 - m$. The divider method is applied for the K_1–K_5 Koch surfaces with α equal to 30° across a large-scale regime, extending from 0.25λ to $3 \times 10^{-4}\lambda$, as shown in Fig. 9. The solid line shows the predicted scaling behavior of K_5 based on the power-law relationship shown in Eq. (13), which relates scaling behavior to α in Koch surfaces, as derived from theoretical analysis by Mandelbrot [51],

$$2(1/3)^D + 2(1/6\cos\alpha)^D = 1. \tag{13}$$

For given Koch curve parameters, surfaces generated with varying numbers of iterations exhibit the same surface fractality (scaling behavior) as represented by D, albeit over varying scale regimes.
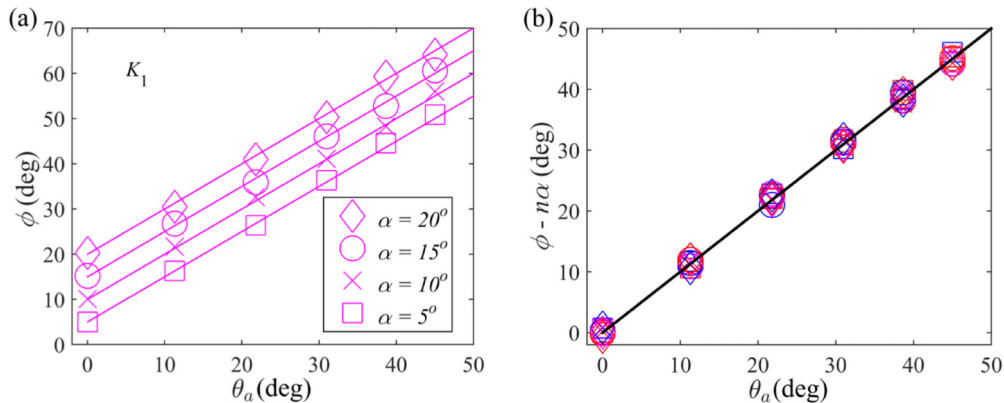

FIG. 8. (Color online) (a) Macroscopic friction angle as a function of atomic friction angle for K_1 surfaces taking different values of α. The solid lines represent the theoretical prediction of $\phi = \theta_a + \alpha$. (b) Plot of $\phi - n\alpha$ (where n is the index of the signature function) against the atomic friction θ_a for $K_0, K_1, K_2,$ and $\alpha = 5°, 10°, 15°,$ and 20°. The data from simulated surfaces collapse into a single line, which demonstrates the robustness of the equation $\phi - n\alpha = \theta_a$.
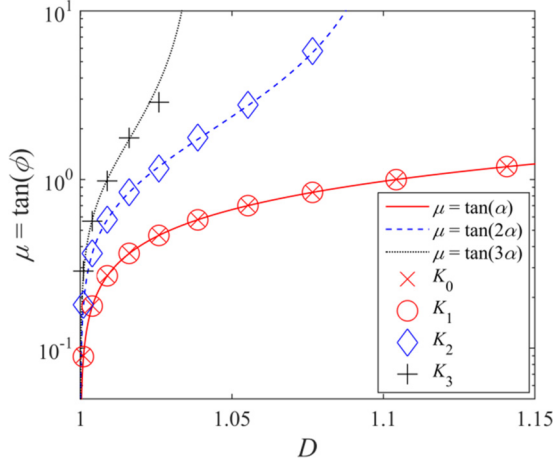
FIG. 10. (Color online) The $\mu - D$ relationships obtained from the simulations and theoretical results.

The variation of μ as a function of D for the Koch surfaces is shown in Fig. 10. This plot indicates that μ increases as D increases. Although the range of D is very small, the results show that fractality is strongly correlated to static friction. This can be understood in light of the increased contact slopes that accompany increasing D.

V. WEIERSTRASS-MANDELBROT FRACTAL SURFACES

In the previous section we utilized idealized fractal surfaces based on Koch curves. These curves capture the non-Euclidian patterns of natural surfaces by complex irregularities that are repeated at a defined number of distinct length scales. To better represent realistic interfaces, the next step is to include the randomness and continuous length-scale distribution of these multiscale irregularities as observed in natural or engineered surfaces.

Beyond Koch surfaces, several fractal surface structures have been discussed and studied in the field of contact mechanics. Here we utilize an Ausloos-Berman-type variant of the Weierstrass-Mandelbrot (WM) function to simulate realistic hierarchical surface profile structures. Following Mandelbrot's definition [51], our Koch surfaces are deterministically self-similar, that is to say, self-similarity is exact. In contrast, the WM surfaces are statistically self-affine, exhibiting different homothetic ratios in different directions with statistical variations. The surface simulation approach employed here yields structures with a highest-level wavelength to account for stochastic processes [31]. Our choice is justified by previous fractal analyses that have been performed on real surfaces such as in magnetic tapes, thin-film rigid disks, steel disks, plastic disks, and diamond films [54]. The fractal description we adopt here has been used in previous studies of friction where friction was related to the shear stress on the real contact area, with simplifications such as rough to flat contact or rigid to elastic-elastic or elastic-plastic contact [55–57]. Here we consider the rough to rough contact of simulated natural surfaces and neglect asperity deformation. This approximation will allow the derivation of signature function to obtain contact slope distributions for varied surfaces, from which different

parameters to describe the friction between fractal surfaces can be extracted.

A. Generation of fractal surface profiles

Following the Ausloos-Berman variants of the WM function, a realistic surface profile with stochastic highest-level features is generated by means of a formula suggested in previous papers [31,58,59],

$$z(x) = G \sum_{n=0}^{n_{max}} \gamma^{2(D-2)n} \left[\cos \phi_n - \cos \left(\frac{2\pi \gamma^n x}{L} + \phi_n \right) \right],$$
(14)

where D controls the fractal dimension, which is between 1 (smooth curves) and 2 (plane filling curves) for two-dimensional (2D) surface profiles. Here L represents the maximum wavelength of the surface. All generated profiles were scaled in the z direction to yield a consistent mean roughness parameter G, which is chosen so that the root mean square of the height of the surface is 0.1% of L. The integer n is a wavelength index number and γ is a parameter that indicates the density of the wavelengths. The commonly used value for γ is 1.5. Given the sufficient number of data points, the greater value of n_{max} provides more fractal detail of the surface profile. In theory, n_{max} should be an infinite number for true fractal surfaces, but in practice it can be a finite value and it has an upper limit of

$$n_{max} = \text{int} \left[\frac{\log(L/L_s)}{\log(\gamma)} \right],$$
(15)

where L_s is the cutoff length that should be greater than the value of smallest wavelength; the notation of int[$\cdots$] returns the maximum integer value for any value in the bracket. For the purpose of numerical studies to investigate the effect of n_{max}, we calculate backward using Eq. (15) to find L_s for a given n_{max}:

$$L_s = L/\gamma^{n_{max}}.$$
(16)

Then the smallest distance between two adjacent data points dx is selected as $L_s/10$ to provide sufficient data for showing the detail of the smallest wavelength, while the dx for the $n_{max} = 0$ case is taken as the same as the dx calculated from $n_{max} = 1$. Here ϕ_n is the random phase that is distributed randomly between 0 and 2π for a stochastic WM function. The deterministic function can be obtained by taking $\phi_n = 0$ in Eq. (14) so that it becomes [31,58]

$$z(x) = G \sum_{n=0}^{n_{max}} \gamma^{2(D-2)n} \left[1 - \cos \left(\frac{2\pi \gamma^n x}{L} \right) \right].$$
(17)

The deterministic function generates surface profiles with an undesired tail at the beginning of the profile. Therefore, in this paper the stochastic function was used. The comparison between the two functions is shown in Fig. 11.

Figure 12 shows the surface profile generated using different values of D. For D values towards 1 we obtain a smooth profile, while $D = 2$ tends towards an area filling profile within the constraints of resolution and amplitude.
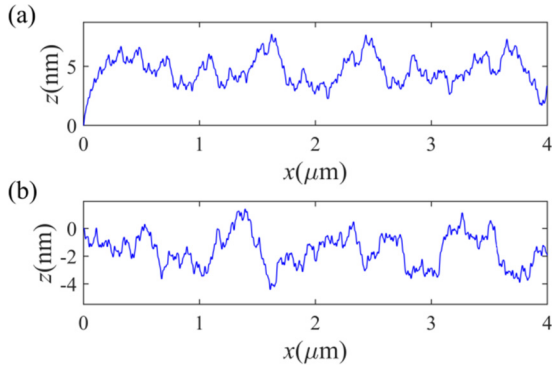
FIG. 11. (Color online) Surfaces generated by (a) deterministic and (b) stochastic WM function for $D = 1.7$ and $n_{max} = 10$.

B. Method of calculation of the contact slope

The signature function is applied to investigate the contact slope between the WM fractal surfaces. The differences of contact slope and surface slope with the surfaces generated from a range of n_{max} and D values are also investigated.

The signature function was calculated in Sec. III for the periodic Koch curve surfaces. To apply the signature function method to calculate the contact slope in the WM fractal surfaces, a few adjustments should be made from the previous method. All surfaces studied here are generated with $L = 1\,\mu\text{m}$ and $L_b = 20\,\mu\text{m}$ (where L_b is the total length of the block). The WM surfaces are generated for $n_{max} = 0\text{--}10$ and the values of L_s can be calculated using Eq. (16). As the mean roughness G is 0.1% of the L, the value of G now is

FIG. 12. (Color online) Typical 2D fractal surfaces with varying fractal dimension from (a) $D = 1.0$ to 1.5 and (b) $D = 1.5$ to 2 at $n_{max} = 10$.
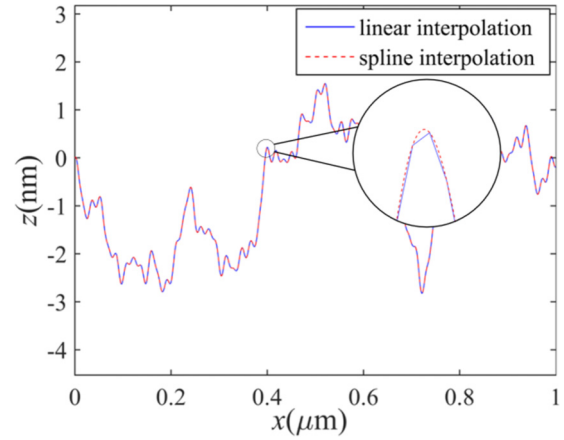

FIG. 13. (Color online) Linear and spline interpolation of the WM fractal surface.

1 nm. Each contacting pair of blocks (upper and lower blocks) would have the same parameters in the WM function except for the random phase ϕ_n, providing the random profiles to be tested. Since the surfaces are nonperiodic, the offset x_{ofs} was varied from zero to half L_b, i.e., $10\,\mu\text{m}$.

Calculating the slope at the contact point for discrete data is another issue. The linear interpolation only provides a rough estimate of the surface slope and contact slope. For the purpose of calculating the slope more precisely for fractal surfaces, a cubic spline interpolation was employed. Plots of linear and spline interpolations are shown and compared in Fig. 13. We check the accuracy of the approximation of slopes by comparing the contact slopes of the upper surface and lower surface at each contact point. Both were approximately the same by using the spline method, thus the contact slope is taken as the average value between them.

C. Surface slope and contact slope

Pairs of fractal surfaces were generated with varying n_{max} and D in the ranges of 0 to 10 and 1 to 2, respectively. We studied the surface slope and contact slope from 20 individual contacting pairs at each n_{max} and D values used. Under the assumption that the surface is rigid, there will be a linear relationship between the static friction coefficient μ and maximum absolute value of contact slope $\tan\theta_{max,\,contact}$, as it has been found in the studies of Koch curve surfaces in the previous section. The maximum absolute values of surface slope $\tan\theta_{max,\,surface}$ and contact slope $\tan\theta_{max,\,contact}$ are studied for each D (from 1 to 2) and n_{max}(from 0 to 10) (Fig. 14). Although the normalization of the height is carried out to yield a constant mean roughness to all surfaces with different fractal dimension, for a given sufficient large value of wavelength index n_{max} the surface slopes increase with D from 1 to 2. The surfaces generated using D between 1.5 and 2 experience a more rapid increase of the surface slope with increasing D, while the surfaces with D less than 1.5 tend to increase at a decreasing rate and have the tendency to converge. Figure 15 shows the trends of both $\tan\theta_{max,\,surface}$ and $\tan\theta_{max,\,contact}$ with the increase of D for $n_{max} = 10$. The rapid growth in surface slope with increasing D is observed in
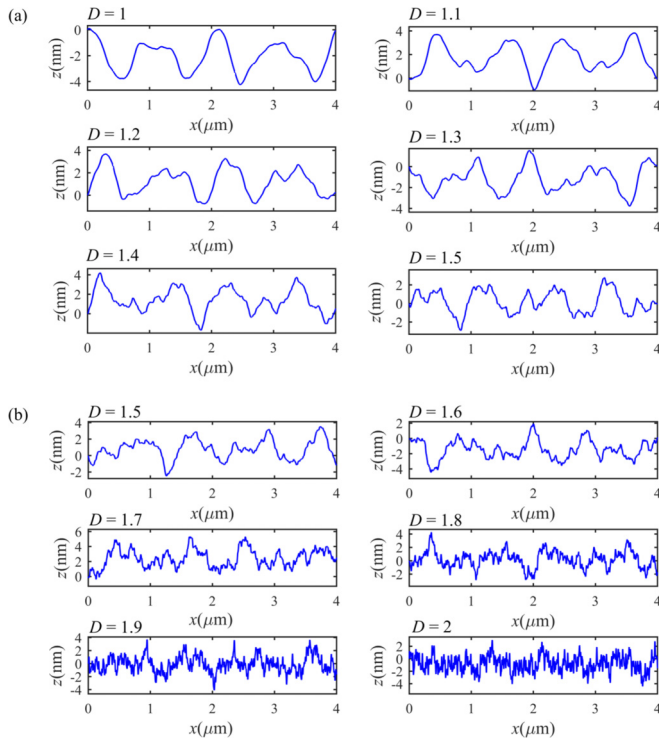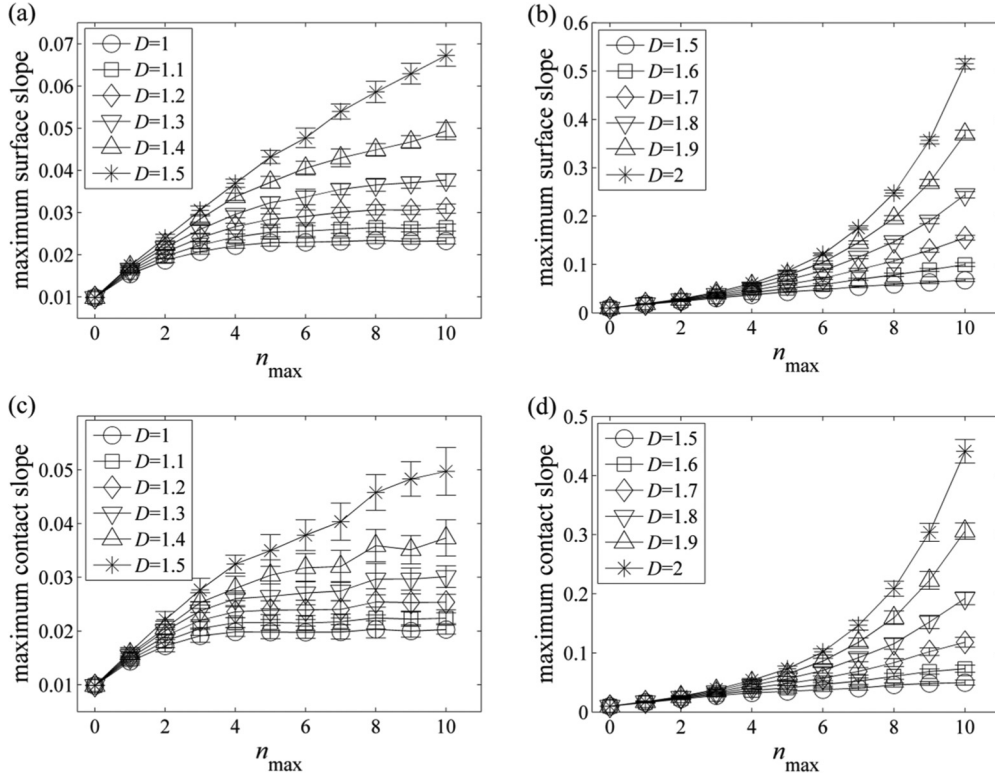
FIG. 14. Maximum surface slope for various D values obtained by varying n_{max}: (a) D varies from 1 to 1.5 and (b) D varies from 1.5 to 2. Maximum contact slope for various D values obtained by varying n_{max}: (c) D varies from 1 to 1.5 and (d) D varies from 1.5 to 2.

the fractal dimension region between 1.5 and 2. The maximum contact slope derived from the surface pair is always smaller than the maximum surface slope but exhibits a similar trend. This is due to the geometrical constraints of the rigid surfaces that hinder the possibility of contact at the asperity with maximum slope.

D. Statistical fluctuations of the static friction

The maximum contact slope provides us with the upper bound of the static friction we can achieve between the surfaces. In practice, the measure of static friction changes every time the experiment is repeated, so one needs to provide

FIG. 15. (Color online) Maximum surface slope and contact slope, at $n_{max} = 10$, for different D values.

a range for the static friction. This is because the surfaces may not necessarily reach the maximum contact slope when they slide against each other. Therefore, it is more realistic to replace Eq. (6) by

$$\phi = \theta_a + \theta, \quad \theta_{max} - \sigma \leqslant \theta \leqslant \theta_{max}. \tag{18}$$

It is reasonable to assume that σ is proportional to the standard deviation of the probability density function of all possible contact slopes. To quantify σ we calculate here the statistical distribution of contact slopes. The probability density function of the slope for fractal surfaces with different D is derived using the data from all 20 individual surface pairs. As the density plots for upper and lower surface slopes are almost the same, only the density of the slope of the upper surface is shown here. Both surface slope and contact slope tend to have an approximately normally distributed shape for any n_{max} greater than 2 (Fig. 16). The standard deviation of surface slope $\sigma_{\text{surface slope}}$ and contact slope $\sigma_{\text{contact slope}}$ are plotted with different values of n_{max} and D (Fig. 17). The trends of standard deviation are similar to the plots of the maximal contact slope as shown in Fig. 14.

To study the effect of applied D on the variability of the static friction, the standard deviation of evaluated contact slopes against D is shown in Fig. 18. For applied values of D larger than $\sim$1.5, an increasingly rapid growth of the obtained standard deviation values is observed for both surface and contact slopes. With the rigid assumption, the trend of static friction coefficient between the fractal surface pairs for different D (Fig. 15) has a trend similar to that of $\sigma_{\text{contact slope}}$. The increasing deviation in static friction
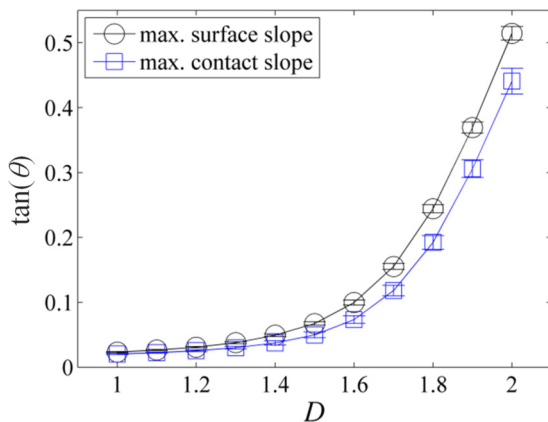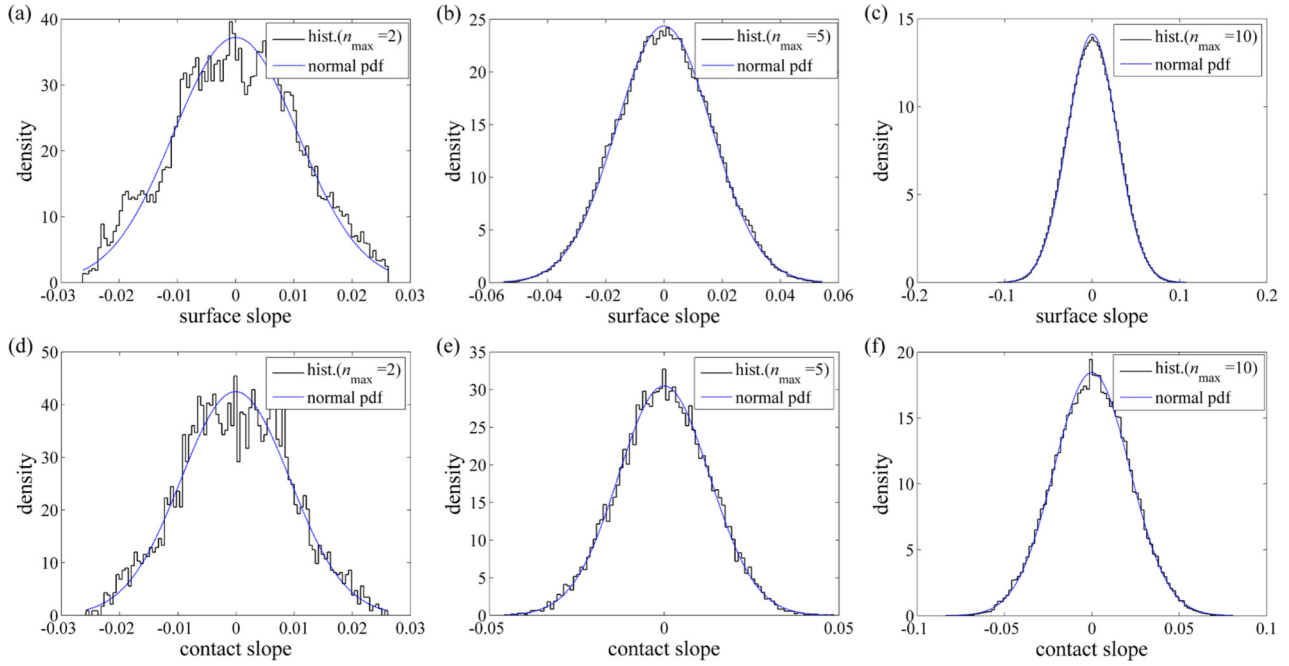
FIG. 16. (Color online) Probability density functions for both (a)–(c) surface slope and (d)–(f) contact slope with $n_{max} = 2$, 5, and 10.

results with increasing fractality of simulated surfaces can be understood in the light of the limited ability to meaningfully represent highly fractal surfaces within the constraints of the simulation resolution.

In summary, we have calculated the maximal value and standard deviation of the angle of apparent friction as a function of the fractal dimension D and the index of the cutoff wavelength n_{max}. We found that both values increase as both D and n_{max} increase. The analysis with the WM functions is more complete than the one of the Koch surfaces, since it provides a measurement of uncertainty on the values of the angle of friction.
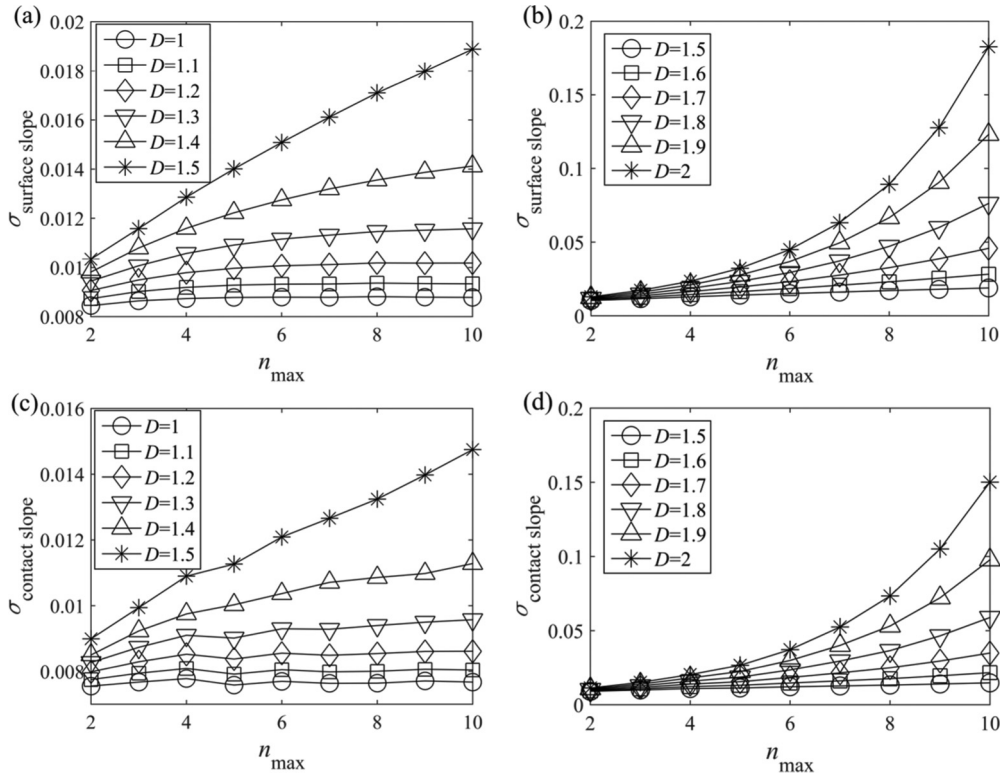

FIG. 17. Standard deviations obtained from the density of slope by varying n_{max} and D for the surface slope [(a) D varies from 1 to 1.5 and (b) D varies from 1.5 to 2] and the contact slope [(c) D varies from 1 to 1.5 and (d) D varies from 1.5 to 2].
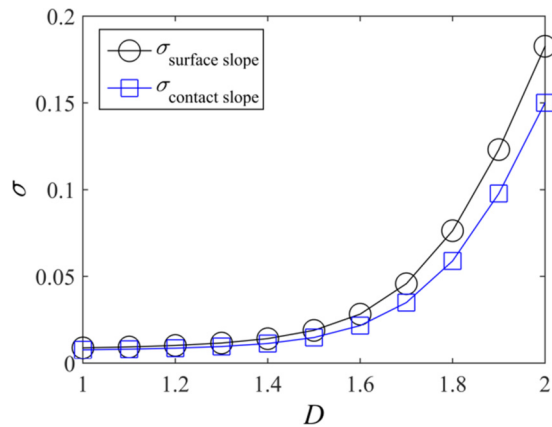
FIG. 18. (Color online) Standard deviation of the contact slope and surface slope against D for $n_{max} = 10$.

VI. CONCLUSION

We derived a theoretical model to determine the static friction coefficient between rigid surfaces. The model describes friction as a superposition of atomic friction and surface roughness. The connection between friction and topography was introduced by means of the signature function. This function returns all possible contact slopes that are compatible with the geometrical constraints of the two rigid bodies. We used a spheropolygon-based numerical method to validate the analytical model. The simulation results are consistent with the analytical model.

Using fractal Koch surfaces, we quantified the effect of topography on static friction by means of simulations and theoretical derivation. The increase of the morphological parameter α, which accounts for the slopes of the asperities on the Koch surface, led to a greater value of friction coefficient. On the other hand, the increase of the number of iterations of the Koch curve generation did not necessarily lead to the increase of the coefficient of friction. Both simulations and theoretical results confirm that small features with large surface slopes do not contribute to the total static friction for cases where these features do not enter contact during translation. Therefore, we conclude that defining compatible contact slopes within the geometrical constraints of the rigid bodies is essential in predicting friction for any pair of surfaces. This was considered in our theoretical model by means of the signature function.

Both simulations and the analytical model demonstrated that large macroscopically observed frictional interactions may arise from changes in the surface morphology. We also noted that the coefficient of friction increases with fractal dimension. This is because the increase of the fractal dimension leads to the increase of the maximal contact slope, which is linearly related to the angle of the static friction.

We extended our analysis to Weierstrass-Mandelbrot-type functions, as they provide a better description than Koch curves for real surfaces. The description of their morphology involves two independent parameters: the applied fractal dimension D and the cutoff wavelength L_s. We found that the maximal contact slope increases as D increases and as L_s decreases. This trend is consistent with the fractal analysis of surfaces found in the literature. Interestingly, the contact slope reaches a finite value as $L_s \to 0$ when $1 < D < 1.5$, whereas it tends to infinity when $1.5 < D < 2$. We also found that in the statistical sense the maximum contact slope is always smaller than maximum surface slope. This means that any estimation of the static friction in rigid surfaces using surface slope will be overestimated and that an accurate description of static friction requires an analysis of the signature function between the two surfaces. Finally, we proposed a formula to predict the upper bound and standard deviation of the static friction in terms of atomic friction and morphology. The latter was achieved by defining two independent morphological parameters: maximum contact slope and standard deviation of the probability density function of contact slopes.

[1] J. Greenwood and J. Williamson, Proc. R. Soc. London Ser. A **295**, 300 (1966).

[2] W. L. Power and T. E. Tullis, J. Geophys. Res. **96**, 415 (1991).

[3] D. A. H. Hanaor, M. Ghadiri, W. Chrzanowski, and Y. Gan, Langmuir **30**, 15143 (2014).

[4] E. Bouchaud, J. Phys.: Condens. Matter **9**, 4319 (1997).

[5] T. Geike and V. L. Popov, Phys. Rev. E **76**, 036710 (2007).

[6] R. Pohrt, V. L. Popov, and A. E. Filippov, Phys. Rev. E **86**, 026710 (2012).

[7] L. Pastewka, N. Prodanov, B. Lorenz, M. H. Müser, M. O. Robbins, and B. N. J. Persson, Phys. Rev. E **87**, 062809 (2013).

[8] J. B. Sokoloff, Phys. Rev. E **73**, 016104 (2006).

[9] J. B. Sokoloff, Phys. Rev. E **85**, 027102 (2012).

[10] G. Carbone and C. Putignano, Phys. Rev. E **89**, 032408 (2014).

[11] P. J. Blau, Tribol. Int. **34**, 585 (2001).

[12] D. A. Hanaor, Y. Gan, and I. Einav, Geotech. Lett. **3**, 52 (2013).

[13] W. Zhong and D. Tomanek, Phys. Rev. Lett. **64**, 3054 (1990).

[14] S. Cheng, B. Luan, and M. O. Robbins, Phys. Rev. E **81**, 016102 (2010).

[15] Y. Mo, K. T. Turner, and I. Szlufarska, Nature (London) **457**, 1116 (2009).

[16] B. Persson, O. Albohr, U. Tartaglino, A. Volokitin, and E. Tosatti, J. Phys.: Condens. Matter **17**, R1 (2005).

[17] Y. Sang, M. Dubé, and M. Grant, Phys. Rev. E **77**, 036123 (2008).

[18] S. Y. Krylov, K. B. Jinesh, H. Valk, M. Dienwiebel, and J. W. M. Frenken, Phys. Rev. E **71**, 065101 (2005).

[19] Y. A. Karpenko and A. Akay, Tribol. Int. **34**, 531 (2001).

[20] D. A. Hanaor, Y. Gan, and I. Einav, Int. J. Solids Struct. **59**, 121 (2015).

[21] J. Archard, Proc. R. Soc. London Ser. A **243**, 190 (1957).

[22] G. Carbone and F. Bottiglione, J. Mech. Phys. Solids **56**, 2555 (2008).

[23] M. Paggi and M. Ciavarella, Wear **268**, 1020 (2010).

[24] S. Hyun, L. Pei, J.-F. Molinari, and M. O. Robbins, Phys. Rev. E **70**, 026117 (2004).

[25] B. N. J. Persson, Phys. Rev. Lett. **89**, 245502 (2002).

[26] N. Myshkin, M. Petrokovets, and A. Kovalev, Tribol. Int. **38**, 910 (2006).

[27] V. A. Yastrebov, G. Anciaux, and J.-F. Molinari, Phys. Rev. E **86**, 035601 (2012).

[28] M. Nosonovsky and B. Bhushan, Mater. Sci. Eng. Rep. **58**, 162 (2007).

[29] F. Bowden and D. Tabor, Proc. R. Soc. London Ser. A **169**, 391 (1939).

[30] F. P. Bowden and D. Tabor, *The Friction and Lubrication of Solids* (Clarendon, Oxford, 1986).

[31] W. Yan and K. Komvopoulos, J. Appl. Phys. **84**, 3617 (1998).

[32] M. Ciavarella, G. Demelio, J. R. Barber, and Y. H. Jang, Proc. R. Soc. London Ser. A **456**, 387 (2000).

[33] Y. F. Gao and A. F. Bower, Proc. R. Soc. London Ser. A **462**, 319 (2006).

[34] Y. Dong, H. Gao, A. Martini, and P. Egberts, Phys. Rev. E **90**, 012125 (2014).

[35] M. Reinstädtler, U. Rabe, V. Scherer, U. Hartmann, A. Goldade, B. Bhushan, and W. Arnold, Appl. Phys. Lett. **82**, 2604 (2003).

[36] B. Bhushan, J. N. Israelachvili, and U. Landman, Nature (London) **374**, 607 (1995).

[37] C. M. Mate, G. M. McClelland, R. Erlandsson, and S. Chiang, Phys. Rev. Lett. **59**, 1942 (1987).

[38] M. A. Lantz, S. J. O'Shea, M. E. Welland, and K. L. Johnson, Phys. Rev. B **55**, 10776 (1997).

[39] F. F. Ling, Tribol. Trans. **32**, 497 (1989).

[40] J. C. Russ, *Fractal Surfaces* (Plenum, New York, 1994).

[41] C. W. Lung, J. Jiang, E. K. Tian, and C. H. Zhang, Phys. Rev. E **60**, 5121 (1999).

[42] L. Pournin and T. M. Liebling, in *Powders and Grains 2005*, edited by R. García-Rojo, H. J. Herrmann, and S. McNamara (Balkema, Stuttgart, 2005), Vol. II, p. 1375.

[43] F. Alonso-Marroquin, Europhys. Lett. **83**, 14001 (2008).

[44] F. Alonso-Marroquín, Á. Ramírez-Gómez, C. González-Montellano, N. Balaam, D. A. H. Hanaor, E. A. Flores-Johnson, Y. Gan, S. Chen, and L. Shen, Granul. Matter **15**, 811 (2013).

[45] F. Alonso-Marroquín and Y. Wang, Granul. Matter **11**, 317 (2009).

[46] S. A. Galindo-Torres, J. D. Muñoz, and F. Alonso-Marroquín, Phys. Rev. E **82**, 056713 (2010).

[47] M. Acevedo, R. C. Hidalgo, I. Zuriguel, D. Maza, and I. Pagonabarraga, Phys. Rev. E **87**, 012202 (2013).

[48] F. Alonso-Marroquín, J. Busch, C. Chiew, C. Lozano, and Á. Ramírez-Gómez, Phys. Rev. E **90**, 063305 (2014).

[49] S. A. Galindo-Torres and D. M. Pedroso, Phys. Rev. E **81**, 061303 (2010).

[50] M. Boton, E. Azéma, N. Estrada, F. Radjai, and A. Lizcano, Phys. Rev. E **87**, 032206 (2013).

[51] B. B. Mandelbrot, *The Fractal Geometry of Nature* (Freeman, San Francisco, 1983).

[52] R. Andrle, Geomorphology **5**, 131 (1992).

[53] C. Aviles and C. Scholz, J. Geophys. Res. **92**, 331 (1987).

[54] S. Ganti and B. Bhushan, Wear **180**, 17 (1995).

[55] M. Renouf, F. Massi, N. Fillot, and A. Saulot, Tribol. Int. **44**, 834 (2011).

[56] B. N. Persson, Surf. Sci. Rep. **61**, 201 (2006).

[57] C. Putignano, L. Afferrante, G. Carbone, and G. Demelio, J. Mech. Phys. Solids **60**, 973 (2012).

[58] M. V. Berry and Z. V. Lewis, Proc. R. Soc. London Ser. A **370**, 459 (1980).

[59] M. Ausloos and D. H. Berman, Proc. R. Soc. London Ser. A **400**, 331 (1985).